



# 3D network mesoporous *beta*-manganese dioxide: Template-free synthesis and supercapacitive performance

Jun-Jie Zhu <sup>a, c</sup>, Li-Li Yu <sup>b, \*</sup>, Jing-Tai Zhao <sup>b, c, \*</sup>

<sup>a</sup> Key Laboratory of Transparent Opto-Functional Inorganic Materials of Chinese Academy of Sciences, Shanghai Institute of Ceramics, 1295 Dingxi Road, Shanghai 200050, PR China

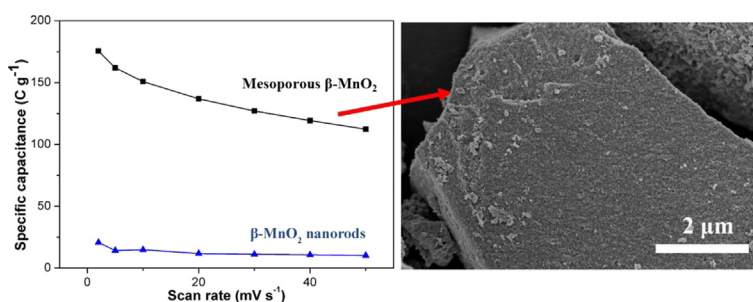
<sup>b</sup> School of Material Science and Engineering, Shanghai University, 149 Yanchang Road, Shanghai 200072, PR China

<sup>c</sup> University of Chinese Academy of Sciences, Beijing 100049, PR China

## HIGHLIGHTS

- A room-temperature and template-free method to form mesoporous  $\beta$ - $\text{MnO}_2$  is presented.
- Obtained  $\beta$ - $\text{MnO}_2$  have high specific surface areas and narrow pore size distributions.
- Mesoporous  $\beta$ - $\text{MnO}_2$  exhibits superior electrochemical performance.

## GRAPHICAL ABSTRACT



## ARTICLE INFO

### Article history:

Received 4 May 2014

Received in revised form

10 July 2014

Accepted 15 July 2014

Available online 23 July 2014

### Keywords:

Manganese dioxide

Supercapacitor

Mesoporous metal oxide

Template-free approach

## ABSTRACT

Sponge-like mesoporous *beta*-manganese dioxide ( $\beta$ - $\text{MnO}_2$ ) with a high specific surface area and narrow pore size distributions has been successfully synthesized at room temperature by a template-free approach. As a supercapacitor electrode, the as-prepared 3D network  $\beta$ - $\text{MnO}_2$  exhibits greatly improved electrochemical performance: not only its specific capacitance enhances from  $\sim 15 \text{ F g}^{-1}$  (traditionally hydrothermal synthesized hollow  $\beta$ - $\text{MnO}_2$  nanorods) to  $\sim 180 \text{ F g}^{-1}$  in 1 M  $\text{Na}_2\text{SO}_4$  aqueous solutions, but also  $\sim 99\%$  of its initial specific capacitance can retain after charge/discharge for 10000 cycles. In addition, its rate retention can maintain at  $\sim 65\%$  as the scan rate increasing from  $2 \text{ mV s}^{-1}$  to  $50 \text{ mV s}^{-1}$ . These results demonstrate that, through modification or improvement,  $\beta$ - $\text{MnO}_2$  can also be a promising electrode material for supercapacitors.

© 2014 Elsevier B.V. All rights reserved.

## 1. Introduction

With the deterioration of environmental and depletion of fossil fuels, the exploration and development of new energy become urgent. In this context, supercapacitors have attracted many

researchers' interest for its combined characteristics of both rechargeable batteries and dielectric capacitors, which make them regarded as one of the most promising candidates for next-generation energy storage systems. Many materials have been used as possible supercapacitor electrodes, such as carbonaceous materials [1], conducting polymers [2] and metal oxides [3–7]. Among them, metal oxide materials have received intensive attention for their high capacitance and fast redox kinetics, such as ruthenium oxide ( $\text{RuO}_2$ ), which exhibits an extremely high capacitance of  $740 \text{ F g}^{-1}$  [7]. However, the high cost and toxicity

\* Corresponding authors. School of Material Science and Engineering, Shanghai University, 149 Yanchang Road, Shanghai 200072, PR China.

E-mail addresses: [lly522@shu.edu.cn](mailto:lly522@shu.edu.cn) (L.-L. Yu), [jtzha@mail.sic.ac.cn](mailto:jtzha@mail.sic.ac.cn) (J.-T. Zhao).

characteristics inhibit its practical applications. Therefore, many efforts have been turned to environmental friendly and inexpensive transition metal oxides, such as NiO [3,4], Co<sub>3</sub>O<sub>4</sub> [5,6] and MnO<sub>2</sub> [8–12].

Among them, MnO<sub>2</sub> is considered to be one of the most promising supercapacitor electrode materials due to its high theoretical capacitance (1370 F g<sup>-1</sup>, 0.9 V voltage windows), low cost, natural abundance and environmental friendliness [13]. Intensive studies have been carried out on its synthesis and/or properties, especially on  $\alpha$ -MnO<sub>2</sub> and  $\delta$ -MnO<sub>2</sub> due to their superior electrochemical performance among the various polymorphs of MnO<sub>2</sub> phases (such as  $\alpha$ ,  $\beta$ ,  $\gamma$ ,  $\delta$  and  $\lambda$ ) [8–12]. The better electrochemical performance of them is considered to relate to their structure nature, 1D 2 × 2 tunnel structure of  $\alpha$ -MnO<sub>2</sub> and 2D layered structure of  $\delta$ -MnO<sub>2</sub>, which promote the electrode kinetics [9,10]. From this point of view,  $\beta$ -MnO<sub>2</sub> with 1D 1 × 1 tunnel structure is not fit for supercapacitor due to the poor kinetics [9], while it has been greatly studied as a lithium or sodium battery material [14–17]. Previous studies have shown that, as a supercapacitor electrode, the specific capacitance of  $\beta$ -MnO<sub>2</sub> is only about 7 F g<sup>-1</sup>, which is far lower than those of  $\alpha$ -/ $\delta$ -MnO<sub>2</sub> (~300 F g<sup>-1</sup>) [8,10,11]. However, lately a 2D  $\beta$ -MnO<sub>2</sub> nanowire network reported by Wei et al. exhibited a special high specific capacitance of ~382 F g<sup>-1</sup> at a scanning rate of 2 mV s<sup>-1</sup> [18], which is quite competitive with  $\alpha$ -/ $\delta$ -MnO<sub>2</sub>. This result suggests that, through improving its electrochemical properties,  $\beta$ -MnO<sub>2</sub> can also be a promising supercapacitor electrode material. Therefore, it is significant and indispensable to investigate  $\beta$ -MnO<sub>2</sub> as a supercapacitor electrode.

According to the charge/discharge storage mechanism of pseudocapacitors, the supercapacitive storage process of MnO<sub>2</sub> mainly includes two sections: (1) the surface adsorption/desorption of electrolyte cations, (MnO<sub>2</sub>)<sub>surface</sub> + M<sup>+</sup> + e<sup>-</sup> ↔ (MnOOM)<sub>surface</sub>; (2) the intercalation/deintercalation of electrolyte cations in the bulk, MnO<sub>2</sub> + M<sup>+</sup> + e<sup>-</sup> ↔ (MnOOM), where M<sup>+</sup> represents proton or metal cations, such as H<sup>+</sup>, Na<sup>+</sup>, K<sup>+</sup> and so on. And the surface adsorption is the main reaction in the whole charge/discharge storage process [19]. Therefore, the specific capacitance, in essence, is mainly produced by the effective utilization of the active material, which can be spurred by the large specific surface area and more access to the interior parts of the porous structure. Recently, porous electrode materials, especially the mesoporous electrode materials, have been proved to show better capacitance behavior, such as mesoporous carbons [20], mesoporous NiO [3] and mesoporous Co<sub>3</sub>O<sub>4</sub> [6]. Since such a porous structure can not only offer a large specific surface area, which enhances the specific capacitance of active materials, but also provide more opportunities to make electrolyte ions more efficiently contacting more active sites for its charge/discharge storage and prevent the deformation or cracking of the crystal lattice, which promotes its rate capability and cycling stability [21]. Consequently, mesoporous structure with a large specific surface area is predicted to significantly improve the capacitive performance of  $\beta$ -MnO<sub>2</sub> as well. However, no literature has reported on mesoporous  $\beta$ -MnO<sub>2</sub> supercapacitor to our best knowledge. In addition, the preparation of mesoporous  $\beta$ -MnO<sub>2</sub> is usually by template methods [15,22], which introduce heterogeneous impurities and low productivity, and increase the production cost and complexity.

Recently, we successfully prepared mesoporous  $\alpha$ -MnO<sub>2</sub> and hierarchical porous  $\beta$ -MnO<sub>2</sub> nanoflowers with high specific surface areas in a simple glucose/KMnO<sub>4</sub> system, whose electrochemical properties can be comparable with those of  $\alpha$ -MnO<sub>2</sub> with high-performance [23]. Herein, we present 3D network mesoporous  $\beta$ -MnO<sub>2</sub> in the mannitol/KMnO<sub>4</sub> system and explore their capacitive behavior. For comparison, 1D hollow  $\beta$ -MnO<sub>2</sub> nanorods were also prepared by using the previously reported hydrothermal methods [16,24].

## 2. Experimental

### 2.1. Synthesis of mesoporous $\beta$ -MnO<sub>2</sub>

All chemicals are of analytical grade and used without further purification. Typically, 50 mL of 0.0075 M KMnO<sub>4</sub> solution were gradually added into 200 mL of 0.0015 M mannitol solution. After constant stirring for 1 h, a number of brown precipitates appeared. Then the precipitates were washed with DI water and dried overnight in air at 80 °C. Finally, 3D network mesoporous  $\beta$ -MnO<sub>2</sub> was obtained (named as S-1).

For comparison,  $\beta$ -MnO<sub>2</sub> hollow nanorods were synthesized by a conventionally hydrothermal method [24]. In a typical process, 35 mL of 0.04 M of KMnO<sub>4</sub> aqueous solution was added to 35 mL of 0.06 M of MnCl<sub>2</sub> aqueous solution. After keeping stirring for 30 min, the mixture was transferred into a 100 mL Teflon-lined stainless steel autoclave, sealed and maintained at 180 °C for 48 h. After cooling down to room temperature, the product was washed repeatedly with DI water, and dried overnight in air at 80 °C. Finally, 1D hollow  $\beta$ -MnO<sub>2</sub> nanorods were got, named as S<sub>rod</sub>.

### 2.2. Material characterization

X-Ray diffraction (XRD) analysis was performed on the as-prepared products with Rigaku Ultima IV X-Ray Diffractometer. Transmission electron microscopy (TEM) was carried out using a JEOL JEM-2100F TEM operated at 200 kV. And the morphologies of the prepared products were examined by scanning electron microscopy (SEM), using a FEI Magellan 400 microscope. The nitrogen adsorption and desorption experiments were carried out at 77 K by means of V-Sorb 2800P Surface Area and Pore Size Analyzers. The specific surface area (SSA) was calculated using the Brunauer–Emmett–Teller (BET) method in the relative pressure range of 0.05–0.25 for MnO<sub>2</sub>. Pore-size distributions (PSDs) were calculated by the Barrett–Joyner–Halenda (BJH) plots using the nitrogen desorption isotherm. The pore width was obtained at the peak of PSD curve. The thermal properties of the samples were studied by simultaneous thermogravimetric and differential scanning calorimetric analysis (TG–DSC) using NETZSCH STA 409 PC thermal analyzer.

### 2.3. Electrochemical characterization

The working electrodes were fabricated by mixing the active material, carbon black and polyvinylidene fluoride (PVDF) at a weight ratio of 80:15:5. Typically, the mixture was first formed to slurry by adding a few drops of 1-methyl-2-pyrrolidinone, then coated onto a stainless steel grid with an apparent area of 1 × 1 cm, and finally dried under vacuum at 80 °C for 12 h. The loading mass of active material was about 2 mg cm<sup>-2</sup>. The prepared electrodes were impregnated with a 1 M Na<sub>2</sub>SO<sub>4</sub> aqueous solution before the electrochemical tests. The electrochemical characterization of the prepared MnO<sub>2</sub> electrodes was carried out with a Bio-logic SP-150 electrochemical working station in a three-electrode cell system. The prepared electrode, a Pt wire and an Ag/AgCl cell were used as working, counter and reference electrodes, respectively. The electrochemical impedance spectroscopy (EIS) was measured at the open-circuit potential over the frequency range of 10<sup>5</sup> to 0.02 Hz with an a.c. amplitude of 5 mV.

## 3. Results and discussion

### 3.1. Physical and chemical characterizations

As shown in Fig. 1, the as-prepared sample S-1 undergoes a 15% weight loss from room temperature to 180 °C with an endothermic

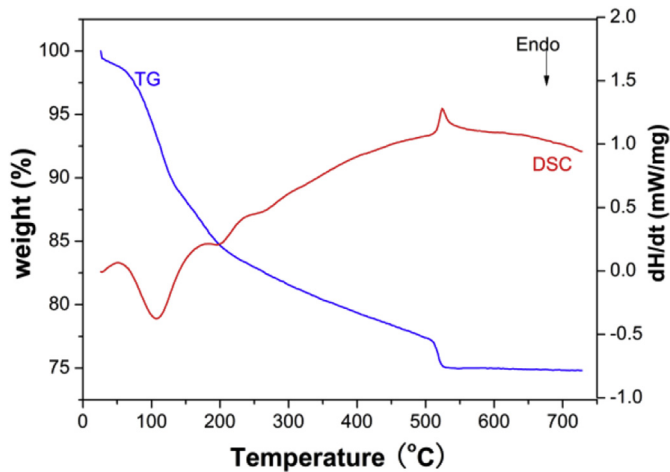


Fig. 1. TG and DSC curves of the as-prepared sample S-1.

peak at 120 °C in its DSC curve, indicating the dehydration of the sample. The exothermic peak at around 520 °C with a slight decrease in weight (3 wt.%), is due to the loss of oxygen from  $\text{MnO}_2$  lattice, which results in a phase transition from  $\text{MnO}_2$  to  $\text{Mn}_2\text{O}_3$  [25]. This is proved by the XRD pattern of sample S-1-550 (S-1 heated at 550 °C in air for 3 h). As shown in Fig. 2(c), characteristic peaks of  $\text{Mn}_2\text{O}_3$  (JCPDS 41-1442) marked with asterisks appear and become the main phase in the sample S-1-550. And associating with the XRD pattern of sample S-1-400 (S-1 heated at 400 °C in air for 3 h) (Fig. 2(b)), we can confirm that the as-prepared sample S-1 is  $\beta\text{-MnO}_2$  (JCPDS No. 24-0735), while its XRD pattern (Fig. 2(a)) is weak and broad, which is common for nanocrystals, indicating a small crystalline particle size. Differently, as shown in Fig. 2(d), the sample  $S_{\text{rod}}$  prepared by the conventional methods [14,24], presents sharp and narrow peaks, which match well with those of  $\beta\text{-MnO}_2$  (JCPDS No. 24-0735), indicating the good crystallization of the sample. In addition, the difference of the main peaks in the samples S-1 and  $S_{\text{rod}}$  implies their different morphologies, which are proved by their BET results and field-effect scanning electron microscopy (FESEM) images (see following analysis).

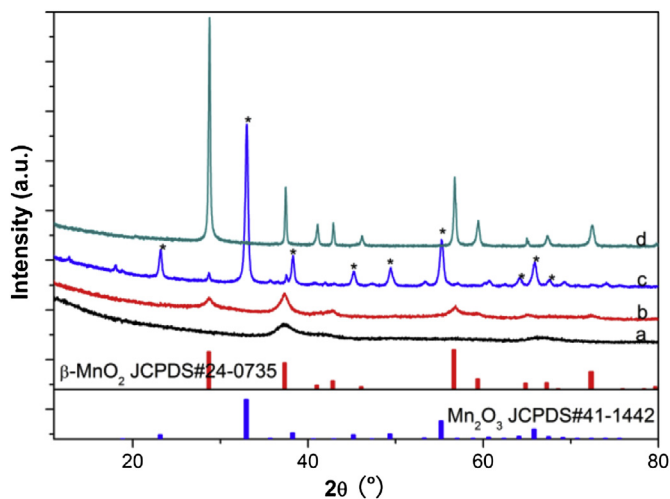


Fig. 2. XRD patterns of the samples S-1(a), S-1 heated at 400 °C (b, named as S-1-400) and 550 °C (c, named as S-1-550) in air for 3 h, respectively, and  $S_{\text{rod}}$  (d). Peaks marked with asterisks belong to  $\text{Mn}_2\text{O}_3$  (JCPDS No. 41-1442).

Fig. 3 shows the nitrogen adsorption–desorption isotherms and BJH pore-size distributions of the samples S-1, S-1-400 and  $S_{\text{rod}}$ . As shown in Fig. 3(a-1), the isotherm of the as-prepared sample S-1 is classified as type IV with an H2-type loop according to the IUPAC classification, indicating a typical mesoporous material with relatively uniform channel-like pores [26]. This is in accordance with its BJH results and FESEM images. As shown in Fig. 3(a-1) inset, the pore size distributions (PSDs) of the samples S-1, calculated using the desorption curve in the context of the BJH method, are narrow and center at around 5.0 nm. Differently, the sample  $S_{\text{rod}}$ , presents type IV isotherm with an H4-type loop (Fig. 3(b)), revealing that it is a typical mesoporous materials with large mesopores embedded in a matrix with pores of much smaller size [27]. This is proved by its PSDs. As shown in Fig. 3(b) inset, two broad and weak peaks centered at around 2.7 nm and 90.1 nm are clearly seen, indicating its hierarchical porous structure, which is in agreement with its FESEM and TEM images (see Figs. 4f and 5b). In addition, the similar nitrogen adsorption–desorption isotherm and BJH pore size distributions (peak centered at 8.6 nm) are found in sample S-1-400 (Fig. 3(a-2)), indicating the thermal stability of the mesoporous structure of sample S-1. This is proved by their FESEM and TEM images (see Fig. 4(a–d) and Fig. 5). The specific surface areas calculated by BET method of samples S-1, S-1-400 and  $S_{\text{rod}}$  are 199.7, 97.8 and 3.1  $\text{m}^2 \text{g}^{-1}$ , respectively, indicating the higher

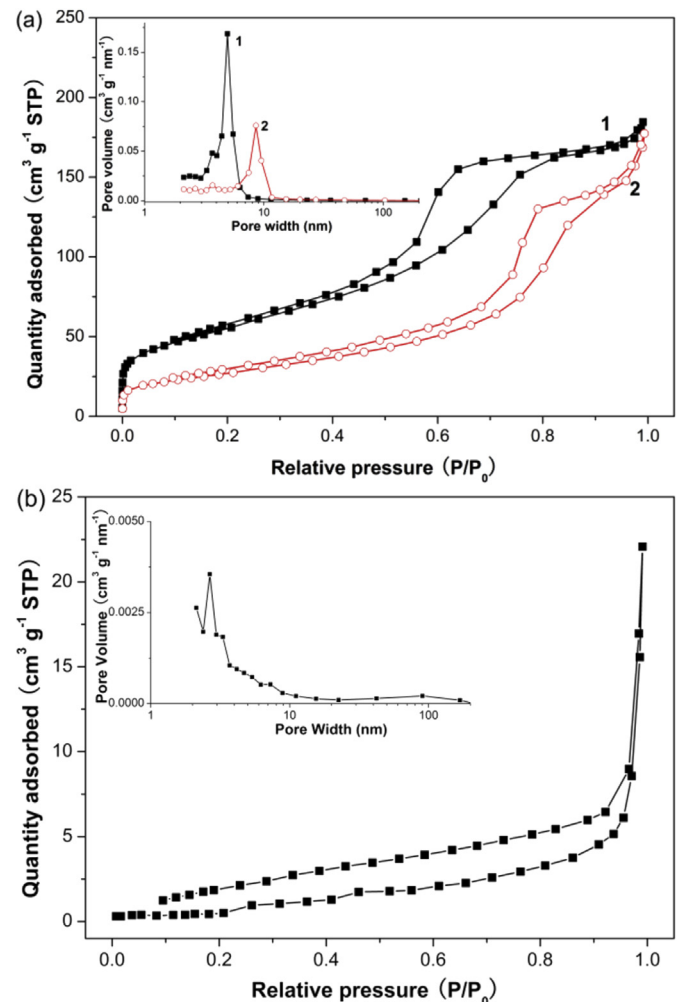
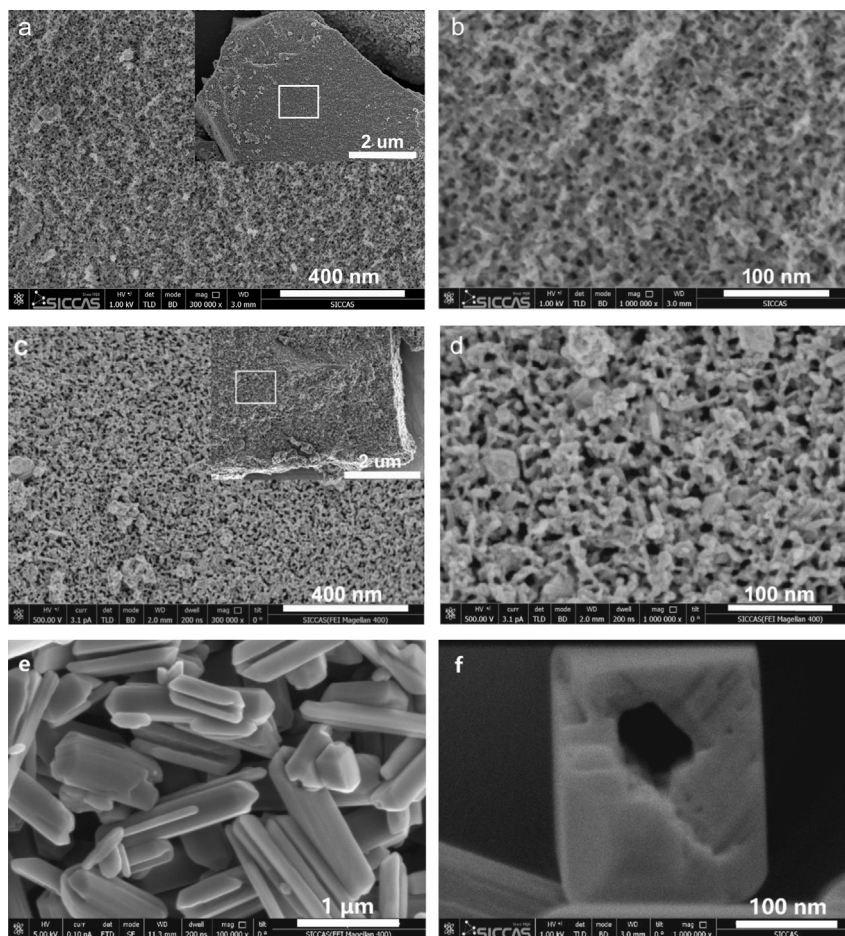


Fig. 3. Nitrogen adsorption–desorption isotherms and BJH pore-size distribution curves (inset) of the samples S-1(a-1), S-1-400 (a-2) and  $S_{\text{rod}}$  (b).





**Fig. 4.** FESEM images of the samples S-1 (a,b), S-1-400 (c,d) and S<sub>rod</sub> (e,f).

specific capacitance of sample S-1. More details are summarized in Table 1.

Fig. 4 shows the FESEM micrographs of samples S-1, S-1-400 and S<sub>rod</sub> at different magnifications. As shown in Fig. 4(a–b), spongy-like morphology with relatively uniform pores randomly distributed in all directions to form 3D networks is clearly seen in sample S-1. Similar morphology can be seen in sample S-1-400 (Fig. 4(c)) except for the larger pores. As shown in Fig. 4(d), larger particles interconnecting to form 3D networks with larger pores

are clearly seen in sample S-1-400. These results are in agreement with their BET results. And according to their transmission electron microscopy (TEM) images, the change of the microstructures of samples S-1 and S-1-400 is considered to relate to the agglomeration during heating process. As shown in Fig. 5(b), larger pores with more crystallized particles are found in sample S-1-400 as compared with sample S-1 (Fig. 5(a)). This is in accordance with their FESEM and XRD results. And the larger particles of sample S-1-400 presented in Fig. 4(b) are derived from the aggregation of

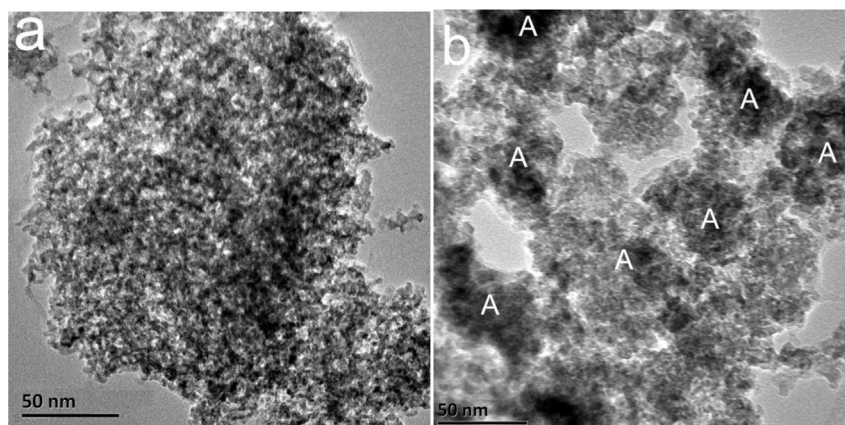


**Fig. 5.** TEM images of samples S-1 (a) and S-1-400 (b). The aggregated particles are marked with "A".

**Table 1**  
Microstructures and electrochemical properties of  $\beta$ -MnO<sub>2</sub> nanomaterials for supercapacitors.

| Reference | Microstructure  | Specific surface area (m <sup>2</sup> g <sup>-1</sup> ) | Average pore size (nm) | Specific capacitance (F g <sup>-1</sup> ) | Electrolyte (Na <sub>2</sub> SO <sub>4</sub> ) |
|-----------|---|---|------------------------|---|--|
| [28]      | $\beta$ -MnO <sub>2</sub> rod   | —   | —                      | 6.33 (1 A g <sup>-1</sup> )               | 0.5 M  |
| [28]      | $\beta$ -MnO <sub>2</sub> wire  | —   | —                      | 9 (1 A g <sup>-1</sup> )                  | 0.5 M  |
| [8]       | $\beta$ -MnO <sub>2</sub> nanowire                                    | 1.0   | —                      | 5 (5 mV s <sup>-1</sup> )                 | 0.1 M  |
| [18]      | 2D $\beta$ -MnO <sub>2</sub> nanowire networks                        | —   | —                      | 381.2 (2 mV s <sup>-1</sup> )             | 1 M  |
| This work | $\beta$ -MnO <sub>2</sub> hollow nanorods (S <sub>rod</sub> )         | 3.1   | 15.4                   | 14.9 (2 mV s <sup>-1</sup> )              | 1 M  |
| This work | 3D $\beta$ -MnO <sub>2</sub> networks with mesoporous structure (S-1) | 199.7   | 4.8                    | 175.4 (2 mV s <sup>-1</sup> )             | 1 M  |
| This work | S-1-400   | 97.8  | 8.3                    | 121.3 (2 mV s <sup>-1</sup> )             | 1 M  |

small crystallized particles, which can be clearly seen in Fig. 5(b) marked with “A”. Moreover, it is noted that the crystallized particle's sizes of samples S-1 and S-1-400 are almost the same, which demonstrates the correctness of above conclusion and confirms the good thermal stability of the mesoporous structure of as-prepared sample S-1. Differently, the sample S<sub>rod</sub> presents a similar nanorod morphology [24]. As shown in Fig. 4(e) and 1D hollow nanorods partly embedded in a matrix with pore sizes less than 15 nm are clearly seen. Connected with Fig. 4(f), the 1D hollow  $\beta$ -MnO<sub>2</sub> nanorods have diameters of 300–400 nm with pore sizes of 50–100 nm. These results are in accordance with its BET test.

### 3.2. Electrochemical performance

To explore the potential application in supercapacitors, the as-prepared mesoporous  $\beta$ -MnO<sub>2</sub> powders were used to make supercapacitor electrodes, and characterized with cyclic voltammetry (CV), galvanostatic charge/discharge (GC) in 1 M Na<sub>2</sub>SO<sub>4</sub> aqueous solutions in a fixed voltage window of  $-0.05$ – $0.85$  V vs. Ag/AgCl. For comparison, 1D hollow  $\beta$ -MnO<sub>2</sub> nanorods (sample S<sub>rod</sub>) were tested as well.

Fig. 6(a) shows the CV curves of samples S-1, S-1-400 and S<sub>rod</sub> at the scan rate of  $10 \text{ mV s}^{-1}$ . Nearly ideal rectangular shape of the CV curves is clearly seen in samples S-1, S-1-400 and S<sub>rod</sub>, indicating their ideal electrical double-layer capacitance behavior and fast charging/discharging process characteristics. And compared with sample S-1, the separation between leveled anodic and cathodic current at the same scan rate of sample S<sub>rod</sub> is quite small, indicating its lower specific capacitance. This is in agreement with their constant-current galvanostatic (GV) charge/discharge results. As shown in Fig. 6(b), the charge/discharge time at a current density of  $1 \text{ A g}^{-1}$  of as-prepared samples changes as following order: S-1 > S-1-400 > S<sub>rod</sub>, indicating the highest specific capacitance of sample S-1. Meanwhile, the similarly symmetric GV charge/discharge curves suggest that all samples S-1, S-1-400 and S<sub>rod</sub> have a good electrochemical capacitive characteristics and superior reversible redox reaction. In addition, as shown in Fig. 6(b), the very slight voltage drops, called IR loss derived from the internal resistance of capacitor [29], are observed at the beginning of the discharge curves of the three samples, indicating their low internal resistance.

The specific capacitances derived from CV curves at different scan rates of them are summarized in Fig. 6(c). The specific capacitance (SC) is calculated using the equation:

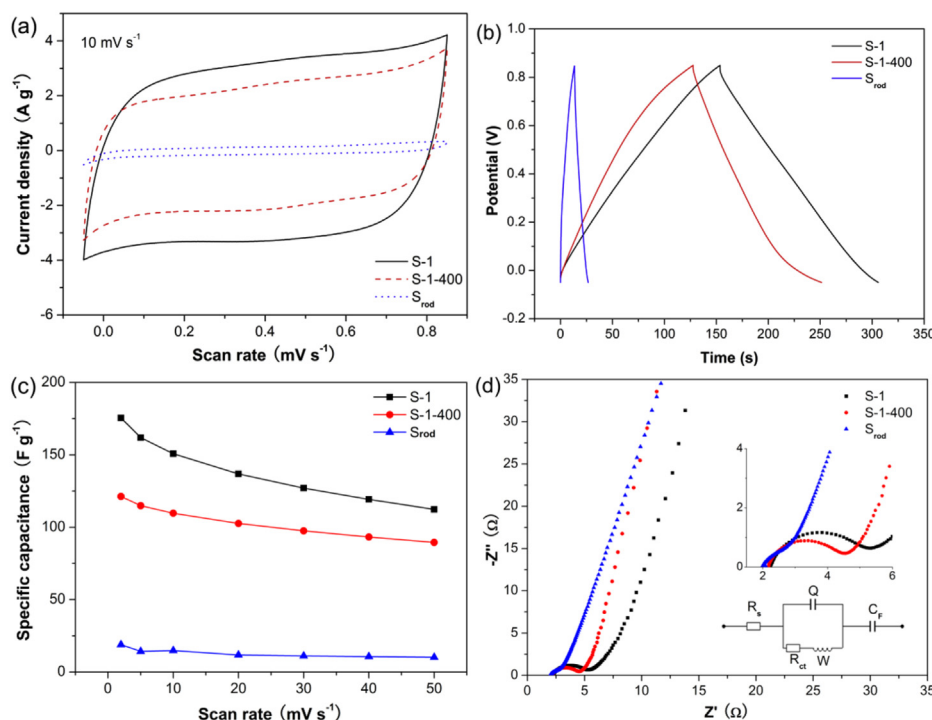


**Fig. 6.** (a) CV curves of the samples S-1, S-1-400 and S<sub>rod</sub> at the scan rate of  $10 \text{ mV s}^{-1}$ ; (b) Galvanostatic charge–discharge curves of the samples S-1, S-1-400 and S<sub>rod</sub> at a current density of  $1 \text{ A g}^{-1}$ ; (c) Specific capacitances of the samples S-1, S-1-400 and S<sub>rod</sub> at different scan rates; (d) Nyquist plots of the samples S-1, S-1-400 and S<sub>rod</sub> electrodes. Inset is the corresponding equivalent circuit.

$$SC = \frac{1}{2m\nu\Delta V} \int i(V)dV$$

where  $m$  is the active weight of the electrode material,  $\nu$  is the scan rate, and  $\Delta V$  is the magnitude of potential range. Notably, the specific capacitances of samples S-1 and S-1-400 at the scan rate of  $2 \text{ mV s}^{-1}$  are  $175.4 \text{ F g}^{-1}$  and  $121.3 \text{ F g}^{-1}$ , respectively, which are 10.8 and 7.1 times higher than that of sample  $S_{\text{rod}}$  ( $14.9 \text{ F g}^{-1}$ ). These values are also larger than many previous reported literatures (see Table 1) [28,30]. The greatly enhanced specific capacitances of samples S-1 and S-1-400 are considered to relate to their larger specific surface areas. As shown in Table 1, the specific surface areas of the samples S-1, S-1-400 and  $S_{\text{rod}}$  increase in order:  $S_{\text{rod}} < S\text{-1-400} < S\text{-1}$ , correspondingly a linear increase specific capacitance change of them. This nearly linear relationship between surface area and specific capacitance also applies to previous reported samples in Table 1, and is in agreement with many literatures of mesoporous materials, such as  $\alpha\text{-MnO}_2$  [21,31], NiO [3,4] and carbon [1,32]. According to the present storage mechanism of pseudocapacitors, electrode materials with large specific surface area can provide more active sites, which generate larger number of redox reactions during the storage process, resulting in higher current density of sample S-1 and/or sample S-1-400 as compared to that of sample  $S_{\text{rod}}$  at the same scan rate. Furthermore, it is noted that the rate retentions of samples S-1, S-1-400 and  $S_{\text{rod}}$  as the scan rate increasing from  $2 \text{ mV s}^{-1}$  to  $50 \text{ mV s}^{-1}$  are 64.7%, 73.8% and 68.6%, respectively, which is not linear change with their crystallization (Fig. 2), indicating their complex kinetic storage process.

Electrochemical impedance spectroscopy (EIS) measurements are characterized to study the storage kinetics of all as-prepared materials. As shown in Fig. 6(d), the EIS of samples S-1, S-1-400 and  $S_{\text{rod}}$  are composed of a partially overlapped semicircle and a straight sloping line, which can be fitted by an equivalent circuit shown in the inset of Fig. 6(d) (details seen Supplementary materials, Fig. S1). It is noted that for all samples, at very high frequency, the intercepts (equal to  $R_s$ , representing the equivalent series resistance) at real part  $Z'$  are almost the same, indicating the same combination resistance of ionic resistance of electrolyte, intrinsic resistance of active materials and contact resistance at the active material/current collector interface [32]. The semicircles at high frequency (corresponding to the Faradic charge transfer resistance ( $R_{\text{ct}}$ )) are changed in the order of  $S\text{-1} > S\text{-1-400} > S_{\text{rod}}$ , which is in accordance with the order of their crystallinity derived from XRD patterns, suggesting that, in present case, the  $R_{\text{ct}}$  mainly arises from the discontinuity in the charge transfer process, due to the conductivity difference between the solid oxide and the electrolyte liquid [33]. With the frequency decreasing, the slope of  $45^\circ$  portion in the transitory frequency next to the noticeable linear part at low frequency region of the respective Nyquist plots represents the diffusive resistance (Warburg impedance,  $W$ ) of the electrolyte in the electrode pores and the proton diffusion in active materials [34], which vary in the order of  $S\text{-1} \approx S\text{-1-400} \ll S_{\text{rod}}$ , indicating lower ion diffusive resistance of sample S-1 (Supplementary material, Table S1). The linear parts at the low frequency region represent the Faradic pseudocapacitance ( $C_F$ ) of the electrode, which change in the order of  $S\text{-1}$  ( $\sim 170 \text{ F g}^{-1}$ )  $>$   $S\text{-1-400}$  ( $\sim 5 \text{ F g}^{-1}$ )  $>$   $S_{\text{rod}}$  ( $\sim 5 \text{ F g}^{-1}$ ) (Supplementary material, Table S1). The extremely small pseudocapacitance value implies the absence of bulk charge/discharge reaction of sample  $S_{\text{rod}}$  in the storage process.

From the above analyses, it is readily to comprehend the difference of their electrochemical properties in the charge/discharge storage process. For the sample  $S_{\text{rod}}$ , while it has good conductivity and hollow structure, the thicker walls make only the surface absorption reaction happen during its charge/discharge storage

process, which results in its very low specific capacitance, due to its low specific surface area (Table 1). Differently, for the sample S-1, the 3D interconnecting mesoporous networks constructed with nanoscale particles lead the electrolyte efficiently flood into the pores of the network structure and decrease the polarization of the electrode, resulting in the increase of its specific capacitance and high-rate capability. These are in accordance with their CV results (Fig. 6(c) and Table 1). With improving its conductivity through heat-treatment, the rate capability of sample S-1-400 is further promoted. This is the reason why sample S-1-400 has the highest rate retention in the mentioned three samples, while its conductivity is not the best (XRD patterns, Fig. 1). Consequently, the existence of the rich mesopores is also the main factor in promoting the high-rate capability of active materials, besides of the conductivity. In addition, the porous existence is favorable to suppress the degradation of active materials, since such a structure can provide an extra space for the diffusion of electrolytes and reduce the stress caused by the cracking of the crystal lattice during the storage process [35].

Cycling stability or cycling life is an important requirement for supercapacitor applications. As shown in Fig. 7, the cycling stabilities of S-1 and  $S_{\text{rod}}$  were evaluated by CV test at a scan rate of  $10 \text{ mV s}^{-1}$  for 10000 cycles. Notably, the specific capacitance of sample S-1 increases slightly ( $\sim 3\%$ ) in the first 500 cycles then retains near constant. After 2500 cycles, its specific capacitance begins to decrease. Fortunately, only  $\sim 2\%$  specific capacitance decreases after 5000 cycles (100.4%), and still 99.1% remains after 10000 cycles. This phenomenon demonstrates the great cycle stability of sample S-1. The slight increase of the specific capacitance is mainly due to the porous microstructure which can provide substantially larger spatial clearance for electrode expansion and contraction during cycling. These expansion and contraction open new active sites within the porous structure in prolonged cycling, which participates in the charge storage process and increases the capacitance value [36]. The similar phenomenon has been reported in earlier literatures [37]. As for  $S_{\text{rod}}$ , a sharp decrease of the specific capacitance was seen in the first 800 cycles. After 10000 cycles, it can only maintain  $\sim 38\%$  of its initial specific capacitance, suggesting its poor cycle stability. Obviously, the mesoporous structure tolerates the electrode expansion and contraction during the storage process, which improves its cycle stability, such as as-prepared sample S-1.

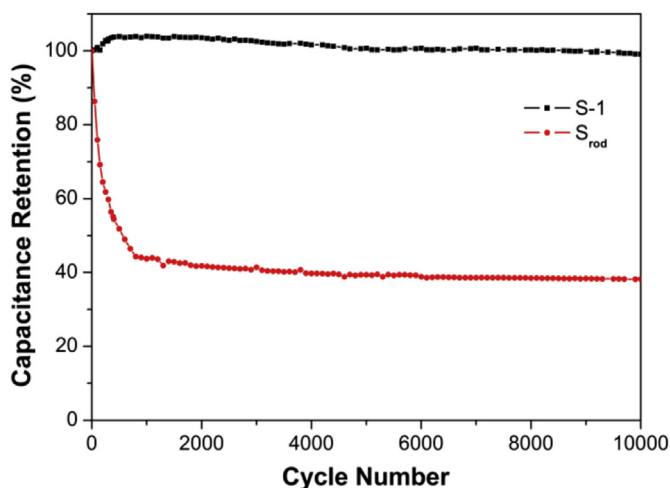


Fig. 7. Charge/discharge cycling life tests of samples S-1 and  $S_{\text{rod}}$  at a scan rate of  $10 \text{ mV s}^{-1}$ .



#### 4. Conclusions

In summary, mesoporous  $\beta$ -MnO<sub>2</sub> is fabricated at room temperature by a template-free method. Due to its high specific surface area and proper pore size distributions, the as-prepared 3D network  $\beta$ -MnO<sub>2</sub> shows a distinctly improved electrochemical performance, e.g. greatly enhanced specific capacitance (~10 times more than traditionally synthesized hollow  $\beta$ -MnO<sub>2</sub> nanorods), improved rate performance (~65%) and good cycling stability, making it as a promising electrode material for supercapacitors. In addition, these results suggest that microstructures, such as specific surface area, pore size and etc., besides of the crystal structure, are the key influences on the electrochemical performance of MnO<sub>2</sub> or metal oxides, and give researchers some inspiration to study the materials which are considered to be lack desirable electrochemical properties.

#### Acknowledgment

This work was financially supported by the National Natural Science Foundation of China (50990304).

#### Appendix A. Supplementary data

Supplementary data related to this article can be found at <http://dx.doi.org/10.1016/j.jpowsour.2014.07.093>.

#### References

- [1] E. Frackowiak, F. Beguin, Carbon 39 (2001) 937–950.
- [2] A. Rudge, J. Davey, I. Raistrick, S. Gottesfeld, J.P. Ferraris, J. Power Sources 47 (1994) 89–107.
- [3] Y.G. Wang, Y.Y. Xia, Electrochim. Acta 51 (2006) 3223–3227.
- [4] H. Pang, Y.F. Shi, J.M. Du, Y.H. Ma, G.C. Li, J. Chen, J.S. Zhang, H.H. Zheng, B.Q. Yuan, Electrochim. Acta 85 (2012) 256–262.
- [5] T. Zhu, J.S. Chen, X.W. Lou, J. Mater. Chem. 20 (2010) 7015–7020.
- [6] S.L. Xiong, C.Z. Yuan, M.F. Zhang, B.J. Xi, Y.T. Qian, Chem. Eur. J. 15 (2009) 5320–5326.
- [7] C.C. Hu, K.H. Chang, M.C. Lin, Y.T. Wu, Nano Lett. 6 (2006) 2690–2695.
- [8] S. Devaraj, N. Munichandraiah, J. Phys. Chem. C 112 (2008) 4406–4417.
- [9] O. Ghodbane, J.L. Pascal, F.d.r. Favier, ACS Appl. Mater. Interfaces 1 (2009) 1130–1139.
- [10] Y.J. Zhang, C.T. Sun, P. Lu, K.Y. Li, S.Y. Song, D.F. Xue, CrystEngComm 14 (2012) 5892–5897.
- [11] L. Su, L. Gong, H. Lu, Q. Xu, J. Power Sources 248 (2014) 212–217.
- [12] W.Y. Ko, L.J. Chen, Y.H. Chen, W.H. Chen, K.M. Lu, J.R. Yang, Y.C. Yen, K.-J. Lin, J. Phys. Chem. C 117 (2013) 16290–16296.
- [13] H.Y. Lee, J.B. Goodenough, J. Solid State Chem. 144 (1999) 220–223.
- [14] F.Y. Cheng, J.Z. Zhao, W. Song, C.S. Li, H. Ma, J. Chen, P.W. Shen, Inorg. Chem. 45 (2006) 2038–2044.
- [15] F. Jiao, P.G. Bruce, Adv. Mater. 19 (2007) 657–660.
- [16] X.K. Huang, D.P. Lv, Q.S. Zhang, H.T. Chang, J.L. Gan, Y. Yang, Electrochim. Acta 55 (2010) 4915–4920.
- [17] D.W. Su, H.J. Ahn, G.X. Wang, J. Mater. Chem. A 1 (2013) 4845–4850.
- [18] C.Z. Wei, H. Pang, B. Zhang, Q.Y. Lu, S. Liang, F. Gao, Sci. Rep. 3 (2013) 2193–2196.
- [19] M. Toupin, T. Brousse, D. Belanger, Chem. Mater. 16 (2004) 3184–3190.
- [20] A.B. Fuertes, F. Pico, J.M. Rojo, J. Power Sources 133 (2004) 329–336.
- [21] Y. Gu, J.W. Cai, M.Z. He, L.P. Kang, Z.B. Lei, Z.H. Liu, J. Power Sources 239 (2013) 347–355.
- [22] J.Y. Luo, J.J. Zhang, Y.Y. Xia, Chem. Mater. 18 (2006) 5618–5623.
- [23] a) L.L. Yu, J.J. Zhu, J.T. Zhao, Eur. J. Inorg. Chem. 2013 (2013) 3719–3725; b) L.L. Yu, J.J. Zhu, J.T. Zhao, J. Mater. Chem. A 2 (2014) 9353–9360.
- [24] X. Huang, D. Lv, H. Yue, A. Attia, Y. Yang, Nanotechnology 19 (2008) 225606–225613.
- [25] Y.S. Ding, X.F. Shen, S. Sithambaram, S. Gomez, R. Kumar, V.M.B. Crisostomo, S.L. Suib, M. Aindow, Chem. Mater. 17 (2005) 5382–5389.
- [26] M. Kruk, M. Jaroniec, Chem. Mater. 13 (2001) 3169–3183.
- [27] H.P. Lin, S.T. Wong, C.Y. Mou, C.Y. Tang, J. Phys. Chem. B 104 (2000) 8967–8975.
- [28] K.F. Chen, Y.D. Noh, K.Y. Li, S. Komarneni, D.F. Xue, J. Phys. Chem. C 117 (2013) 10770–10779.
- [29] G. Xiong, K.P.S.S. Hembram, R.G. Reifemberger, T.S. Fisher, J. Power Sources 227 (2013) 254–259.
- [30] Z.H. Yang, Z.S. Mei, F.F. Xu, Y.J. Yao, W.X. Zhang, W.C. Qi, Q.L. Song, Z.W. Gao, T. Zhao, J. Mater. Sci. 48 (2013) 2512–2519.
- [31] J.P. Ma, Q.L. Cheng, V. Pavlinek, P. Saha, C.Z. Li, New. J. Chem. 37 (2013) 722–728.
- [32] J. Gamby, P.L. Taberna, P. Simon, J.F. Fauvarque, M. Chesneau, J. Power Sources 101 (2001) 109–116.
- [33] S.K. Meher, G.R. Rao, J. Power Sources 215 (2012) 317–328.
- [34] M. Kim, Y. Hwang, J. Kim, J. Power Sources 239 (2013) 225–233.
- [35] G. Wang, B. Zhang, J.R. Wayment, J.M. Harris, H.S. White, J. Am. Chem. Soc. 128 (2006) 7679–7686.
- [36] R. Ranjusha, A.S. Nair, S. Ramakrishna, P. Anjali, K. Sujith, K.R.V. Subramanian, N. Sivakumar, T.N. Kim, S.V. Nair, A. Balakrishnan, J. Mater. Chem. 22 (2012) 20465–20471.
- [37] Y. Zhang, G.Y. Li, Y. Lv, L.Z. Wang, A.Q. Zhang, Y.H. Song, B.L. Huang, Int. J. Hydrogen Energy 36 (2011) 11760–11766.